

Manuscript Template

FRONT MATTER

Title

Design of Ru-Ni diatomic sites for efficient alkaline hydrogen oxidation

Authors

Lili Han^{1†}, Pengfei Ou^{2†}, Wei Liu^{3†}, Xiang Wang⁴, Hsiao-Tsu Wang⁵, Rui Zhang¹, Chih-Wen Pao⁶, Xijun Liu^{3*}, Way-Faung Pong⁵, Jun Song², Michael V. Mirkin⁴, Jun Luo³, Huolin L. Xin^{1*}

Affiliations

- ¹ Department of Physics and Astronomy, University of California, Irvine, CA 92697, USA.
- ² Department of Mining and Materials Engineering, McGill University, Montreal H3A 0C5, Canada.
- ³ Institute for New Energy Materials & Low-Carbon Technologies and Tianjin Key Lab of Photoelectric Materials & Devices, School of Materials Science and Engineering, Tianjin University of Technology, Tianjin 300384, China.
- ⁴ Department of Chemistry and Biochemistry, Queens College CUNY, Flushing, New York 11367, United States.
- ⁵ Department of Physics, Tamkang University, New Taipei City 25137, Taiwan.
- ⁶ National Synchrotron Radiation Research Center, Hsinchu 30076, Taiwan.
- *Corresponding author. Email: xjliu@tjut.edu.cn (X.J.L.); huolin.xin@uci.edu (H.L.X.)

†These authors contributed equally to this work.

Abstract

The kinetics of alkaline hydrogen oxidation reaction (HOR) which plays a significant role in cost-effective anion exchange membrane fuel cells is limited by lack of catalysts with high-efficiency active sites for the HOR. Here, we establish HOR catalytic activities of single-atom and diatomic sites as a function of H* binding energy to screen the optimal active sites for the HOR. Among the screened sites, the Ru-Ni diatomic one is identified as the best active center. Guided by the theoretical finding, we subsequently synthesize a catalyst with Ru-Ni diatomic sites supported on N-doped porous carbon, which exhibits excellent catalytic activity, CO tolerance, and stability for alkaline HOR, and is also superior to single-site counterparts and commercial Pt/C. In-situ scanning electrochemical microscopy study validates the HOR activity resulting from the Ru-Ni diatomic sites. Further, in-situ X-ray absorption spectroscopy and computational studies unveil a synergistic interaction between Ru and Ni to promote the molecular H2 dissociation and strengthen OH adsorption at the diatomic sites, and thus enhance the kinetics of HOR.

MAIN TEXT

Anion exchange membrane fuel cells (AEMFCs) enabling conversion of chemical energy directly into hydrogen energy in alkaline media have gained significant attention because of the possibility to use economical electrocatalysts, bipolar plates, air loops, and membranes (1, 2). Hydrogen oxidation reaction (HOR) plays a significant role in AEMFC. Unfortunately, HOR kinetics are quite slow in alkaline media. For example, the HOR activity on noble metals (e.g. Pt, Pd and Ir) drop approximately 100-fold when the electrolyte goes from acid to base (3–6). Attempting to address such limitation, a number variety of strategies have been developed for low-cost and high-performance alkaline HOR electrocatalysts, such as alloying two metals (7–10), preparing core—shell structures (11–13), engineering hybrid nanostructures (5, 14, 15), tuning the crystalline structures of the metals (16, 17), among others (18). Despite the great progress mentioned above in promoting the HOR activity, it is still a great challenge to precisely design cost-effective electrocatalysts with high-efficiency active sites for alkaline HOR.

Besides the well-known Pt (3–5), prior studies on pure metals suggest Ru (19, 20), Ni (21, 22), Pd (4), and Ir (3) as the ones exhibiting good performance for alkaline HOR compared to others, attributed to their optimal values of H* binding energy (HBE). In this study, we particularly focus on the single-atom catalysts (SACs) constructed from these metal centers, due to their highest atom-utilization efficiency, unique electronic structures and unsaturated coordination environments of the active centers, and thus superior catalytic performances (23–28). We began with BEEF-vdW calculations on pure metal SACs, and our results revealed that the HBE (ΔG_{*H}) is very strong on Ir and Ru SACs, whereas it is too weak on Pd, Ni, and Pt SACs (table S1). Thus, we considered combining two metal centers separately from these two groups to construct diatomic site catalysts (DASCs) as a possible strategy for effective tuning of ΔG_{H} . The effect of different combinations between diatomic sites on the energetics of HOR reaction intermediates is first estimated based on the simple linear interpolation argument (Fig. 1A), which has been confirmed to be an effective method of tuning the energetics of oxygen evolution reaction intermediates on metal oxides (29). To validate the interpolation principle, we then extended our calculations to different DASCs, with calculated theoretical $\Delta G_{^*H}$ and its corresponding indicator of HOR activity (i.e., exchange current density, in the unit of A cm⁻²) shown in the two-dimensional (2D) volcano plot of Fig. 1B. As seen in Fig. 1B and table S1, the calculated ΔG_{H} value of a DASC is not exactly at halfway between the combined two endpoint metals (e.g., Pd-Ni, Ru-Ni, Ru-Pt, et al.), indicating inaccuracy of the linear interpolation argument in predicting ΔG_{H} on DASCs. Nonetheless, despite its inaccuracy, we found that the linear interpolation argument can still be used to provide quite rough estimates and qualitative assessment. For instance, two metal centers with weak HBE (positive ΔG_{*H}) combined, e.g., Ni-Pd, would result in a DASC with weak HBE (0.40 eV) and poor HOR activity. The incorporation of a weak HBE metal at a strong HBE metal center results in effective tuning of $\Delta G_{\rm H}$ to a more optimal value (Ru-Ni and Ru-Pt in Fig. 1B, more results in table S1). Overall, our computational screening suggests that Ru-Ni DASC be the best candidate for HOR with a theoretical overpotential of only 0.04 eV among all the screened systems, to promise effective and selective HOR performance.

Based on the theoretical prediction, we synthesized the Ru-Ni diatomic sites supported on N-doped porous carbon (RuNi/NC) via a dissolution-and-carbonization method (28) (see Methods for details). The morphology of the obtained product was characterized by the aberration-corrected high-angle annular dark-field scanning transmission electron microscopy (HAADF-STEM) and scanning electron microscopy (SEM). Fig. 2A and fig. S1A shows that RuNi/NC features three-dimensional interconnected carbon frameworks with randomly opened porous structures. The N₂ adsorption-desorption isotherm and pore distribution in fig. S1B,C demonstrate that RuNi/NC has a high specific area of 320.83 m² g⁻¹ and exists many pores with sizes of 3 ~ 8 nm, which are advantageous for accessibility of active sites and mass transport of electrolytes during electrolysis (26). The X-ray diffraction (XRD) pattern in fig. S1D

demonstrates that RuNi/NC is amorphous, which evidences no Ru- or Ni-related crystals particles in the sample. This result is further confirmed by elemental mapping acquired by the energy-dispersive X-ray spectroscopy (EDS) (Fig. 1B), where Ru, Ni and N homogeneously distribute over the entire architectures and no aggregation exists in the sample. Atomic-resolution HAADF-STEM images in Fig. 1C show that many spot pairs with two different contracts are distributed on the carbon matrix, suggesting the existence of abundant Ru-Ni diatomic pairs on the matrix. The Ru and Ni loadings in RuNi/NC were measured by inductively coupled plasma mass spectrometry (ICP-MS) as 5.05 wt% and 3.57 wt%, respectively.

The X-ray photoelectron spectroscopy (XPS) and X-ray absorption fine structure (XAFS) spectroscopy were employed to explore the local structure of Ru and Ni atoms in RuNi/NC. Fig. 2D shows that compared with Ru/NC, Ru 3d XPS spectrum of RuNi/NC shifts toward a higher energy direction, suggesting the introduction of Ni causes the electronic change of Ru in RuNi/NC. To further determine the coordination environment of Ru and Ni atoms in RuNi/NC, we fit the Ru and Ni K-edge X-ray absorption near edge structure (XANES) and Fourier transform extended XAFS (FT-EXAFS) spectra with RuN₃NiN₃/graphene, RuN₄/graphene and NiN₄/graphene models. As a result, the experimental Ru XANES spectrum match better with the calculated RuN₃NiN₃ one than the calculated RuN₄ one (Fig. 2E). The Ru K-edge FT-EXAFS spectrum also matches well with the fitting curve of the RuN₃NiN₃ model (Fig. 2F and table S2). Moreover, the Ni K-edge XANES and FT-EXAFS spectra are fitted well with the RuN₃NiN₃ model (fig. S1E, F and table S2). Thus, we infer that the RuNi/NC sample is mainly composed of the RuN₃NiN₃ structure rather than the RuN₄ and NiN₄ ones. Such a result is consistent with our models in DFT calculations and the observation of abundant Ru, Ni atomic pairs distributed on the N-doped carbon matrix (Fig. 2B, C).

The control samples (Ru/NC, Ni/NC, and NC) were synthesized via the same method as that of RuNi/NC (see Methods for details). The characterizations in figs. S2 and S3 confirm that the Ru/NC and Ni/NC consist of atomically dispersed Ru and Ni sites supported on the N-doped carbon, respectively. The Ru and Ni loadings in Ru/NC and Ni/NC are determined to be 11.37 wt% and 8.5 wt%, respectively, through ICP-MS measurements.

The HOR performance of the RuNi/NC, Ru/NC, Ni/NC, and NC catalysts was examined in a three-electrode setup with H₂-saturated 0.1M KOH electrolyte. Commercial Johnson Matthey 20 wt% Pt/C was used as reference measurements. The HOR polarization curves in Fig. 3A show that the anodic current density of the RuNi/NC catalyst is higher than those of other catalysts under the whole potential range, indicating the good HOR activity of RuNi/NC. Of note, it is also superior to most of alkaline HOR catalysts (see table S3). According to the Koutecky–Levich equation (21), linear relationships between the inverse of overall current density at an overpotential of 50 mV vs. reversible hydrogen electrode (RHE, all potentials in this work are given vs. RHE unless stated otherwise.) and the reciprocal of square root of the rotation rate has been plotted, which yield slopes of 4.13 cm² mA⁻¹ s^{-1/2} for RuNi/NC, 4.04 cm² mA⁻¹ s^{-1/2} for Ru/NC and, 4.96 cm² mA⁻¹ s^{-1/2} for Ni/NC (fig. S4), close to the theoretical value of 4.87 cm² mA⁻¹ s^{-1/2} for the two-electron transfer of HOR (31).

We obtained the kinetic current density (j_k) for RuNi/NC, Ru/NC and Ni/NC according to the Koutecky–Levich equation (21). To understand the intrinsic HOR activity, we evaluated their mass-specific kinetics current density $(j_{m,k})$, and the values were determined to be 272.85 mA mg $_{RuNi}^{-1}$ for RuNi/NC, 130.17 mA mg $_{Ru}^{-1}$ for Ru/NC and, 82.59 mA mg $_{Ni}^{-1}$ for Ni/NC, indicating the superior intrinsic HOR activity of RuNi/NC than Ru/NC and Ni/NC. To the best of our knowledge, the obtained $j_{m,k}$ value for RuNi/NC outperforms those of the best-reported alkaline HOR catalysts (table S3). A logarithmic function of j_k versus the working potential and their Butler–Volmer fitting²¹ were presented in Fig. 3B. By the fitting, the value

of exchange current density (*j*₀) for RuNi/NC was determined to be 2.75 mA cm⁻² at an overpotential of 50 mV, higher than those on Ru/NC (1.82 mA cm⁻²) and Ni/NC (0.99 mA cm⁻²). By linear fitting of micropolarization regions (from –5 to 5 mV) ⁹, we also identified the exchange current density (*j*₀) (Fig. 3C). As a result, the values are consistent with the counterparts obtained from the Bulter–Volmer fitting (Fig. 3B). These findings demonstrate that RuNi/NC possesses a faster HOR kinetics, compared with Ru/NC and Ni/NC (Fig. 3D). We further examined the HOR activities of the RuNi/NC catalyst in the presence of CO. As shown in Fig. 3E, the RuNi/NC catalyst only has a small decrease of 10 % over the overall current density at 50 mV during HOR electrolysis in the presence of 200 ppm CO, far better than the Pt/C catalyst. The current density for the HOR on RuNi/NC only decreases by 11% after continuous operation for 30 h (Fig. 4F and fig. S5), indicating high electrocatalytic stability.

The catalytic activity of micrometer-sized RuNi/NC toward HOR was mapped in basic 0.1 M phosphate buffer (PB) solution at pH 10 by using a scanning electrochemical microscope (SECM) in the tip generation-substrate collection (TG-SC) mode. We used relatively large nanoelectrodes ($a \sim 250$ nm) for TG-SC mapping since micrometer-sized N-doped porous carbon sheets are relatively large, non-flat, and rough (fig. SxA—SEM image) as compared to the specimens imaged in our previous SECM studies of 2D electrocatalysts.(32–34) In Fig. 4A, the tip electrode was biased at -1.2V (vs. Ag/AgCl) and positioned at a close distance (e.g. comparable to tip radius, a, determined from the SECM negative approach curve at the tip electrode; fig. S1) from the substrate (see Methods section for experimental details). H2 generated at the tip through H₂O/OH⁻ reduction, diffused to and was oxidized at the substrate sample (biased at +0.8 V). The fast HOR at the RuNi-porous C leads to a higher substrate current (~16 pA) than the background current (~15.3 pA) in the TG-SC image, as shown in Fig. 4B. In a control experiment, the activity of the NC sample containing no RuNi was measured using the SECM substrate approach curve in TG-SC mode. When H₂ produced at the tip electrode was not oxidized at the substrate, the substrate current decreased with the tip electrode approaching it due to blocking of H₂ diffusion to its surface. This result can be seen in Fig. 4C, pointing to the immeasurably low activity of the NC sample containing no RuNi.

We also used SECM feedback mode to image the conductivity and HOR activity of RuNi/NC and NC catalysts in acidic solution. In this mode, either Fc/Fc⁺ (fig. S2A) or H⁺/H₂ (fig. S2B) couple was used as the redox mediator. The tip electrode was held at a close distance from the substrate during mapping (see Methods section for experimental details). The feedback mode SECM images in 1 mM Fc solution (fig. S2C, E) were obtained with substrate unbiased. With a Fc redox mediatyor, the tip current was higher (positive feedback, see Methods section for experimental details) above both RuNi/NC and NC than over the surrounding indium tin oxide (ITO) glass due to the fast electron transfer at its surface and high lateral conductivity, consistent with the intrinsic conductive nature of N-doped porous carbon. However, H⁺/H₂ used as the redox mediator (fig. S2B), the positive feedback was only observed over the diatomic RuNi catalyst (fig. S2D) while bare N-doped carbon showed a negative feedback (fig. S2F), indicating that the sample activity for HOR is due to RuNi diatomic sites.

To obtain mechanistic understanding for the superior HOR performance on the RuNi/NC, BEEF-vdW calculations were further conducted to calculate the *OH binding energy (OHBE, ΔG_{*OH}) since the formation of an adsorbed hydroxide (*OH) was suggested to be a key factor in determining the kinetics of HOR under alkaline conditions (35–37). For SACs, we found that the *OH adsorption is much energetically favorable on Ru SAC compared to that of Ni SAC. When alloying Ni SAC with Ru to form RuNi DASC, ΔG_{*OH} can be modified from very weak adsorption (Ni SAC) to a thermal-neutral value (ΔG_{*OH} is 0.05 eV on Ru top in RuNi DASC).

This indicates that the adsorption of *OH is effectively mediated through the heterometallic bonding between Ru and Ni towards a more optimal value. Combined with optimal value of ΔG_{*H} value on Ni top in RuNi DASC, we propose the reaction mechanism for alkaline HOR under low overpotential range: the molecular H₂ first dissociates and adsorbs on the Ni top site, and then the adsorbed *OH on Ru top site reacts with *H to release the H₂O molecules (as illustrated in Fig. 5A). We note that the near thermal-neutral value of ΔG_{*OH} suggests OH coming from the electrolytes can also easily combine with adsorbed *H on Ni top site to further enhance the kinetics of HOR on RuNi DASC.

We then conducted in-situ XAFS measurements at the Ru and Ni K-edge of RuNi/NC during HOR in the H₂-saturated 0.1 M KOH electrolyte to validate the proposed reaction mechanism. Figure 5B shows that the main K-edge peaks of Ru XANES spectra get higher from 0 to 0.1 V and lower from 0.1 to 0.25 V, indicating the increase of unoccupied state of the Ru 5p orbital from 0 to 0.1 V and the decrease from 0.1 to 0.25 V. Interestingly, the first-shell peaks of Ru K-edge FT-EXAFS spectra also have the same trend (Fig. 5C). The increase is contributed by the adsorbed *OH on the Ru top site and the decrease by the *OH desorption to release the H₂O molecule. By contrast, the intensity of the Ni K-edge peak only increases from 0 to 0.05 V and then almost goes back to the original value when over 0.05 V (Fig. 5D), while the first-shell peaks of Ni K-edge FT-EXAFS spectra have almost no change (Fig. 5E). The increase could result from the dissociation of molecular H₂ first dissociates and adsorption on the Ni top site. These findings are consistent with the DFT calculation results in Fig. 5A, and support the proposed mechanism.

Conclusions

To summarize, we developed a design strategy for targeting an optimum HOR catalyst with combined theoretical and experimental efforts, and deepened the understanding of HOR mechanism by in-situ techniques. Starting out, our DFT calculations predict that the Ru-Ni diatomic site is the best active center for the HOR among the screened systems of single-atom and diatomic sites. As a result, the catalyst with the Ru-Ni diatomic sites exhibits excellent HOR activity with current density of 2.03 mA cm⁻², mass-specific kinetic current density of 272.85 mA mg⁻¹_{RuNi}, exchange current density of 2.75 mA cm⁻² at an overpotential of 50 mV in alkaline electrolyte, which is superior to single-site counterparts and most of alkaline HOR catalyst. The catalyst also displays excellent CO tolerance and HOR stability. Scanning electrochemical microscopy study reveals that the superior electrochemical activity of RuNi/NC results from the Ru-Ni diatomic sites. DFT calculations and in-situ X-ray absorption spectroscopy studies further unveil a synergistic interplay between Ru and Ni in promoting molecular H₂ dissociation and strengthening OH adsorption during the HOR.

Methods

Synthesis. In a typical procedure, 144 mg anhydrous glucose (C₆H₁₂O₆), 6.81 mg ruthenium (III) chloride (RuCl₃), 3.19 mg nickel (II) nitrate hexahydrate (H₁₂N₂NiO₁₂) and 690 mg hydroxylammonium chloride ((NH₃OH)Cl) were ultrasonically dissolved in 80 mL of deionized water-ethanol solution (with a volume ratio of 1:1) to form a transparent solution. The solution was placed in a drying oven at 70 °C for 24 h, and the obtained solid was ground into powder, placed in a porcelain boat, heated in a tube furnace to 550 °C with a rate of 5 °C min⁻¹, and carbonized at 550 °C for 4 h under Ar protection atmosphere. The obtained black product was ground into fine powder and denoted as RuNi/NC.

The Ru/NC was prepared with the same procedures as those of RuNi/NC except for only 9.09 mg RuCl₃ but no Ni precursor added.

The Ni/NC was prepared with the same procedures as those of RuNi/NC except for only 12.76 mg H₁₂N₂NiO₁₂ but no Ru precursor added.

The NC was prepared with the same procedures as those of RuNi/NC except for neither Ru nor Ni precursors added.

Characterizations. XRD patterns were collected using an X-ray diffractometer (Rigaku D/max 2500) at a scan rate of 10° min⁻¹ in the 2θ range of $10 \sim 90^{\circ}$. SEM observations were performed using a field-emission-gun (FEG) SEM instrument (Verios 460L of FEI). Low-magnification HAADF-STEM images were recorded using an FEI Talos F200X S/TEM with a FEG. Atomic-resolution HAADF-STEM images and EDS mappings were taken using an FEI Titan Cubed Themis G2 300 S/TEM with a probe corrector. XPS measurements were performed using a Kratos AXIS Ultra DLD system with the Al K α radiation as the X-ray source. N2 sorption/desorption measurements were performed at 77 K using an autosorb iQ instrument (Quantachrome, US) with the Brunauer–Emmett–Teller (BET) method. Pore-size distribution was obtained from the N2 sorption/desorption isotherm. The Ru and Ni K-edge XAFS spectra were recorded at beamline TPS 44A of National Synchrotron Radiation Research Center. Metal contents of the samples were analyzed by inductively coupled plasma mass spectrometry (Thermo Fishier iCAP RQ ICP-MS).

XANES calculation. In this work, we have performed the theoretical XANES calculations to explore the local structures of Ru and Ni elements in RuNi/NC within the FDMNES package in the framework of real-space full multiple-scattering (FMS) scheme with the muffin-tin approximation which is realized by applying Green function in FDMNES. The energy-dependent exchange-correlation potential was calculated in the real Hedin–Lundqvist scheme, and then the XANES spectra were convoluted using a Lorentzian function with an energy-dependent width to account for the broadening from both the core-hole and final-state widths. A cluster of 10.0 Å radius containing ~100 atoms was used in the calculation with satisfactory convergence being achieved. The structural models for XANES fitting were built based on the EXAFS fitting results and were further optimized by DFT. For the simulation of Ni edge, the cut-off of the occupied states and orbit spin are considered.

EXAFS fitting. The EXAFS fitting was performed for the Fourier transformed k²-weighted experimental EXAFS signals using Artemis software. The EXAFS data were preprocessed and normalized in Athena software. Fitting includes both the imaginary and real parts of the Fourier transformed EXAFS oscillations and minimized the difference between the normalized experimental data and the theoretical EXAFS. The multiple-scattering path for the given atomic structure model is calculated using the FEFF8-lite code in Artemis.

Electrochemical test. All electrochemical tests were carried out on an electrochemical workstation (CHI 760E) with a standard three-electrode system under the 0.1 M KOH solution and at room temperature (25 °C). A graphite rod and Hg/HgO electrode were applied as the counter electrode and reference electrode, respectively. The glassy carbon electrode loading catalyst ink was performed as the working electrode. To prepare the catalyst ink, 5 mg of the sample was dispersed in a solution containing 500 μL 0.5 wt% Nafion and 500 μL ethanol, and then the ink was dispersed by ultrasound for at least 30 minutes. After that, 10 μL solution was dropped onto the glassy carbon electrode (0.196 cm⁻² for active geometric area) and dried at room temperature. The catalyst loading of RuNi/NC on the glassy carbon electrode was 0.25 mg cm⁻². As for HOR (hydrogen oxidation reaction) experiments, linear sweep voltammetry (LSV) was tested with sweep rates of 1 mV s⁻¹ at a rotation rate of 1600 rpm in the H₂-saturated electrolytes. 90% iR compensation was applied to all initial data except stability data. The cyclic voltammetry (CV) range is from -0.05 to 0.3 V vs. RHE. The CV was scanned 50 times before scanning LSV.

SECM electrodes and electrochemical experiments: Pt nanoelectrodes with the tip radius (a) ranging from 100 to 250 nm were fabricated by pulling and heat sealing 25 μm diameter Pt wires into borosilicate glass capillaries under vacuum with a P - 2000 laser pipet puller as described previously (38). The fabricated nanoelectrodes were polished on a 50 nm alumina pad (Precision Surfaces International) under video microscopic control. Appropriate protection was used to avoid electrostatic damage to the nanotips (39). The three-electrode setup was used with a commercial Ag/AgCl serving as a reference electrode and a 1 mm Pt wire as a counter electrode. N-doped porous carbon sheets were deposited on the surface of ~6μm diameter carbon fiber microelectrode and ITO glass in basic and acidic experimental conditions, respectively, used as the SECM substrate.

SECM setup and procedures: SECM experiments were carried out using the previously described home-built instrument (32). The tip was brought within a \sim 30 µm vertical distance from the substrate using a manual micromanipulator under an optical microscope. Then, the tip was moved toward the substrate using the z-piezo stage over \sim 25 µm distance with a relatively high approach velocity (e.g., 0.5 µm/s) in the bulk solution, then a slower velocity (e.g., 100 nm/s) was switched in the SECM feedback range (within the range of the diffusion field of the reactant at the tip) to obtain the approach curve and locate substate z position. All experiments were carried out at room temperature inside a Faraday cage.

In SECM feedback approach (i_T vs. d) curve experiment, the tip and substrate current can both be recorded as a function of the distance of the tip from the substrate. When Fc was used as the redox mediator, the tip was biased at a sufficiently positive potential to oxidize Fc at a rate governed by its diffusion (diffusion-limited current, $i_{T,\infty}$, is reached in this case). When the distance between the tip and substrate (d) was sufficiently small (i.e., comparable to tip radius, a), Fc⁺ oxidized at the tip would be reduced back to Fc at the conductive substrate (here RuNi/NC or NC) surface, causing an increase of the tip current with decreasing d. This is called SECM positive feedback; $i_T > i_{T,\infty}$. Otherwise, if Fc⁺ produced at the tip, cannot be effectively reduced back to Fc at the substrate, in other words, the regeneration rate of Fc was slow, i_T would be decreased with decreasing d because of the hindered diffusion of Fc, resulting in a SECM negative feedback approach curve; $i_T < i_{T,\infty}$.

When H⁺ acted as the redox mediator and the source of H₂ in acidic solution, the tip was biased at a negative potential, $E_T = -0.7 \text{ V}$ (vs. Ag/AgCl), to reduce H⁺ (hydrogen evolution reaction, HER) at its surface and the substrate is biased at +0.4V (vs. Ag/AgCl) for HOR. The solution contains 10 mM H₂SO₄ and 0.2 M K₂SO₄. When H₂ came from H₂O/OH⁻ reduction (H₂O or OH⁻ or both) at the tip in basic (pH 10) solution, E_{tip} was biased at -1.2V (vs. Ag/AgCl). In both cases, SECM tip negative feedback approach curves were resulted when the substrate was unbiased or not reactive towards HOR. SECM feedback mode images (Fig. S2C-F) were obtained by scanning the tip laterally (in the x-y plane) over the sample surface at a distance (i.e., comparable to tip radius, a) within the feedback current range.

Another mode of SECM imaging used in this work was tip generation-substrate collection (TG-SC) mode, as shown in Fig. 4A, where H₂ was generated at the tip by H₂O/OH⁻ reduction (H₂O or OH⁻ or both) and diffused to the substrate (here RuNi/NC) and got oxidized (HOR). The potential of the tip and substrate were -1.2 and +0.8 V vs. Ag/AgCl, respectively. Before scanning in TG-SC mode, the tip was first brought close to the unbiased substrate in SECM tip negative feedback experiment where the substrate is unbiased (fig. S1).

In-situ XAFS measurement. The in-situ experiments were conducted at room temperature in a flow half-cell with H₂-saturated 0.1 M KOH electrolyte. The sample was loaded on a glassy carbon electrode and immersed in the electrolyte. The Ru and Ni K-edge XAFS spectra were

recorded at open circuit potential (0 V), 0.05 V, 0.1 V, 0.15 V, and 0.25 V vs. RHE in the fluorescence mode at Beamline TPS 44A of National Synchrotron Radiation Research Center.

Density functional theory calculations. Spin-polarized first-principles calculations based on density functional theory (DFT) (40, 41) were performed using projector-augmented wave (PAW) method (42, 43) as implemented in the Vienna *ab initio* simulation package (VASP) (43). Electron exchange and correlation terms were described by semi-empirical Bayesian error estimation functional with van der Waals (BEEF-vdW) functional (44) that combines generalized gradient approximation with long-range dispersion correction derived from the DFT-D2 method of Grimme (45). The SACs and DASCs were modeled in a 6 × 6 graphene nanosheet, e.g., Ru/NC, Ni/NC, and RuNi/NC were modeled by RuN4, NiN4, and RuN3NiN3 centers, respectively. For all the calculations, a cut-off energy of 500 eV was set and the Brillouin zone was sampled by gamma-centered 2 × 1 × 1 k-points generated by the Monkhorst-Pack scheme. The structural relaxations were covered when the residual force on each ion fell below 0.01 eV Å⁻¹, and the convergence of electronic structure was considered to be reached when the energy difference between two iterations was smaller than 10^{-5} eV per atom. We employed a Fermi-level smearing width of 0.05 eV for the calculations of adsorbates, whereas 0.01 eV for non-adsorbed species, to improve the convergence.

Gibbs free energy corrections for Adsorbates and non-adsorbed species. The Gibbs free energy of H* and OH* binding ($\Delta G_{\text{H*}}$ and $\Delta G_{\text{OH*}}$) were determined by the computational hydrogen electrode (CHE) model (46) where the Gibbs free energy for a proton/electron pair ($G(\text{H}^+ + \text{e}^-)$) in the electrolyte is treated equally to half of the Gibbs free energy of molecular H₂ 0.5 $G(\text{H}_2)$. G was calculated as $G = E + \text{ZPE} + \int C_p dT - TS$, where E is the electronic energy obtained from *ab initio* DFT calculations, ZPE, $\int C_p dT$, and TS are the contributions from zero-point energies, temperature enthalpic, and entropic corrections (T = 300 K), respectively.

Supplementary Materials

table S1. Gibbs free energies of *H and *OH binding on different single-atom catalysts

(SACs) and diatomic site catalysts (DASCs) from BEEF-vdW calculations.

fig. S1. Additional characterizations of RuNi/NC.

table S2. Structural parameters extracted from the EXAFS fittings for the RuNi/NC sample.

fig. S2. Structural characterizations of Ru/NC.

fig. S3. Structural characterizations of Ni/NC.

table S3. Comparison between electrocatalysts for alkaline HOR in prior studies and our work.

fig. S4. HOR polarization curves.

fig. S5. HOR polarization curves of RuNi/NC before and after the 30-h stability test.

References and Notes

- 1. B. P. Setzler, Z. Zhuang, J. A. Wittkopf, Y. Yan, Activity targets for nanostructured platinum-group-metal-free catalysts in hydroxide exchange membrane fuel cells. *Nat. Nanotechnol.* **11**, 1020 (2016).
- 2. Y. Xue, L. Shi, X. Liu, J. Fang, X. Wang, B. P. Setzler, W. Zhu, Y. Yan, Z. Zhuang, A highly-active, stable and low-cost platinum-free anode catalyst based on RuNi for hydroxide exchange membrane fuel cells. *Nat. Commun.* 11, 5651 (2020).
- 3. J. Durst, A. Siebel, C. Simon, F. Hasché, J. Herranz, H. A. Gasteiger, New insights into the electrochemical hydrogen oxidation and evolution reaction mechanism. *Energy Environ. Sci.* 7, 2255–2260 (2014).

- 4. H. A. Miller, A. Lavacchi, F. Vizza, M. Marelli, F. Di Benedetto, F. D'Acapito, Y. Paska, M. Page, D. R. Dekel, A Pd/C-CeO₂ anode catalyst for high-performance platinum-free anion exchange membrane fuel cells. *Angew. Chem. Int. Ed.* **128**, 6108–6111 (2016).
- 5. V. Briega-Martos, A. Ferre-Vilaplana, E. Herrero, J. M. Feliu, Why the activity of the hydrogen oxidation reaction on platinum decreases as pH increases. *Electrochim. Acta* **354**, 136620 (2020).
- 6. L. An, X. Zhao, T. Zhao, D. Wang, Atomic-level insight into reasonable design of metal-based catalysts for hydrogen oxidation in alkaline electrolytes. *Energy Environ. Sci.* **14**, 2620–2638 (2021).
- 7. H. Wang, H. D. Abruña, Rh and Rh alloy nanoparticles as highly active H₂ oxidation catalysts for alkaline fuel cells. *ACS Catal.* **9**, 5057–5062 (2019).
- 8. Y. Wang, G. Wang, G. Li, B. Huang, J. Pan, Q. Liu, J. Han, L. Xiao, J. Lu, L. Zhuang, Pt-Ru catalyzed hydrogen oxidation in alkaline media: oxophilic effect or electronic effect? *Energy Environ. Sci.* **8**, 177–181 (2014).
- 9. S. Lu, Z. Zhuang, Investigating the influences of the adsorbed species on catalytic activity for hydrogen oxidation reaction in alkaline electrolyte. *J. Am. Chem. Soc.* **139**, 5156–5163 (2017).
- 10. G. Wang, W. Li, B. Huang, L. Xiao, J. Lu, L. Zhuang, Exploring the composition-activity relation of Ni-Cu binary alloy electrocatalysts for hydrogen oxidation reaction in alkaline media. *ACS Appl. Energy Mater.* **2**, 3160–3165 (2019).
- 11. B. Qin, H. Yu, J. Jia, C. Jun, X. Gao, D. Yao, X. Sun, W. Song, B. Yi, Z. Shao, A novel IrNi@PdIr/C core-shell electrocatalyst with enhanced activity and durability for the hydrogen oxidation reaction in alkaline anion exchange membrane fuel cells. *Nanoscale*. **10**, 4872–4881 (2018).
- 12. E. Liu, L. Jiao, J. Li, T. Stracensky, Q. Sun, S. Mukerjee, Q. Jia, Interfacial water shuffling the intermediates of hydrogen oxidation and evolution reactions in aqueous media. *Energy Environ. Sci.* **13**, 3064–3074 (2020).
- 13. D. Liu, S. Lu, Y. Xue, Z. Guan, J. Fang, W. Zhu, Z. Zhuang, One-pot synthesis of IrNi@Ir core-shell nanoparticles as highly active hydrogen oxidation reaction electrocatalyst in alkaline electrolyte. *Nano Energy.* **59**, 26–32 (2019).
- 14. Y. Duan, Z. Yu, L. Yang, L. Zheng, C. Zhang, X. Yang, F. Gao, X. Zhang, X. Yu, R. Liu, H. Ding, C. Gu, X. Zheng, L. Shi, J. Jiang, J. Zhu, M. Gao, S. Yu, Bimetallic nickel-molybdenum/tungsten nanoalloys for high-efficiency hydrogen oxidation catalysis in alkaline electrolytes. *Nat. Commun.* 11, 4789 (2020).
- 15. G. Huang, W. Liang, Y. Wu, J. Li, Y. Jin, H. Zeng, H. Zhang, F. Xie, J. Chen, N. Wang, Y. Jin, H. Meng, Co₂P/CoP hybrid as a reversible electrocatalyst for hydrogen oxidation/evolution reactions in alkaline medium. *J. Catal.* **390**, 23–29 (2020).
- 16. C. -P. Huang, M. -C. Tsai, X. -M. Wang, H. -S. Cheng, Y. -H. Mao, C. -J. Pan, J. -N. Lin, L. D. Tsai, T. -S. Chan, W. -N. Su, B. -J. Hwang, Engineering heterometallic bonding in bimetallic electrocatalysts: towards optimized hydrogen oxidation and evolution reactions. *Catal. Sci. Technol.* **10**, 893–903 (2020).
- 17. Y. Qiu, L. Xin, Y. Li, I. T. McCrum, F. Guo, T. Ma, Y. Ren, Q. Liu, L. Zhou, S. Gu, M. J. Janik, W. Li, BCC-phased PdCu alloy as a highly active electrocatalyst for hydrogen oxidation in alkaline electrolytes. *J. Am. Chem. Soc.* **140**, 16580–16588 (2018).
- 18. J. Mao, C. -T. He, J. Pei, Y. Liu, J. Li, W. Chen, D. He, D. Wang, Y. Li, Isolated Ni atoms dispersed on Ru nanosheets: high-performance electrocatalysts toward hydrogen oxidation reaction. *Nano Lett.* **20**, 3442–3448 (2020).
- 19. J. Ohyama, T. Sato, Y. Yamamoto, S. Arai, A. Satsuma, Size specifically high activity of Ru nanoparticles for hydrogen oxidation reaction in alkaline electrolyte. *J. Am. Chem. Soc.* **135**, 8016–8021 (2013).

Science Advances Manuscript Template Page 9 of 16

- 20. Y. Zhou, Z. Xie, J. Jiang, J. Wang, X. Song, Q. He, W. Ding, Z. Wei, Lattice-confined Ru clusters with high CO tolerance and activity for the hydrogen oxidation reaction. *Nat. Catal.* **3**, 454–462 (2020).
- 21. Z. Zhuang, S. A. Giles, J. Zheng, J G. R. enness, S. Caratzoulas, D. G. Vlachos, Y. Yan, Nickel supported on nitrogen-doped carbon nanotubes as hydrogen oxidation reaction catalyst in alkaline electrolyte. *Nat. Commun.* 7, 10141 (2016).
- 22. E. S. Davydova, F. D. Speck, M. T. Y. Paul, D. R. Dekel, S. Cherevko, Stability limits of Nibased hydrogen oxidation electrocatalysts for anion exchange membrane fuel cells. *ACS Catal.* **9**, 6837–6845 (2019).
- 23. S. Ji, Y. Chen, X. Wang, Z. Zhang, D. Wang, Y. Li, Chemical synthesis of single atomic site catalysts. *Chem Rev.* **14**, 2620–2638 (2020).
- 24. Y. Chen, S. Ji, C. Chen, Q. Peng, D. Wang, Y. Li, Single-atom catalysts: synthetic strategies and electrochemical applications. *Joule.* **2**, 1242–1264 (2018).
- 25. L. Han, M. Hou, P. Ou, H. Cheng, Z. Ren, Z. Liang, J.A. Boscoboinik, A. Hunt, I. Waluyo, S. Zhang, L. Zhuo, J. Song, X. Liu, J. Luo, H. L. Xin, Local modulation of single-atomic Mn sites for enhanced ambient ammonia electrosynthesis. *ACS Catal.* 11, 509–516 (2020).
- 26. L. Han, X. Liu, J. Chen, R. Lin, H. Liu, F. Lü, S. Bak, Z. Liang, S. Zhao, E. Stavitski, J. Luo, R. R. Adzic, H. L. Xin, Atomically dispersed molybdenum catalysts for efficient ambient nitrogen fixation. *Angew. Chem. Int. Ed.* **58**, 2321–2325 (2019).
- 27. L. Han, Z. Ren, P. Ou, H. Cheng, N. Rui, L. Lin, X. Liu, L. Zhuo, J. Song, J. Sun, J. Luo, H. L. Xin, Modulating single-atom palladium sites with copper for enhanced ambient ammonia electrosynthesis. *Angew. Chem. Int. Ed.* **60**, 345–350 (2021).
- 28. L. Han, S. Song, M. Liu, S. Yao, Z. Liang, H. Cheng, Z. Ren, W. Liu, R. Lin, G. Qi, X. Liu, Q. Wu, J. Luo, H. L. Xin, Stable and efficient single-atom Zn catalyst for CO₂ reduction to CH₄. *J. Am. Chem. Soc.* **142**, 12563–12567 (2020).
- 29. B. Zhang, X. Zheng, O. Voznyy, R. Comin, M. Bajdich, M. García-Melchor, L. Han, J. Xu, M. Liu, L. Zheng, F. P. G. de Arquer, C. T. Dinh, F. Fan, M. Yuan, E. Yassitepe, N. Chen, T. Regier, P. Liu, Y. Li, P. De Luna, A. Janmohamed, H. L. Xin, H. Yang, A. Vojvodic, E. H. Sargent, Homogeneously dispersed multimetal oxygen-evolving catalysts. *Science*. **352**, 51–51 (2016).
- 30. J. Greeley, T. F. Jaramillo, J. Bonde, I. Chorkendorff, J. K. Nørskov, Computational high-throughput screening of electrocatalytic materials for hydrogen evolution. *Nat. Mater.* **5**, 909–913 (2006).
- 31. W. Sheng, H. A. Gasteiger, Y. Shao-Horn, Hydrogen oxidation and evolution reaction kinetics on platinum: acid vs alkaline electrolytes. *J. Electrochem. Soc.* **157**, B1529 (2010).
- 32. T. Sun, H. Zhang, X. Wang, J. Liu, C. Xiao, S. U. Nanayakkara, J. L. Blackburn, M. V. Mirkin, E. M. Miller, Nanoscale mapping of hydrogen evolution on metallic and semiconducting MoS₂ nanosheets. *Nanoscale Horiz.* **4**, 619–624 (2019).
- 33. A. Djire, X. Wang, C. Xiao, O. C. Nwamba, M. V. Mirkin, N. R. Neale, Basal plane hydrogen evolution activity from mixed metal nitride MXenes measured by scanning electrochemical microscopy. *Adv. Funct. Mater.* **30**, 2001136 (2020).
- 34. T. Sun, D. Wang, M. V. Mirkin, H. Cheng, J. -C. Zheng, R. M. Richards, F. Lin, H. L. Xin, Direct high-resolution mapping of electrocatalytic activity of semi-two-dimensional catalysts with single-edge sensitivity. *Proc. Natl. Acad. Sci.* 116, 201821091 (2019).
- 35. D. Strmcnik, M. Uchimura, C. Wang, R. Subbaraman, N. Danilovic, V. Dennis, A. P. Paulikas, V. R. Stamenkovic, N. M. Markovic, Improving the hydrogen oxidation reaction rate by promotion of hydroxyl adsorption. *Nat. Chem.* **5**, 300–306 (2013).
- 36. R. Subbaraman, D. Tripkovic, K. -C. Chang, D. Strmcnik, A. P. Paulikas, P. Hirunsit, M. Chan, J. Greeley, V.Stamenkovic, N. M. Markovic, Trends in activity for the water electrolyser reactions on 3d M(Ni,Co,Fe,Mn) hydr(oxy)oxide catalysts. *Nat. Mater.* 11, 550–557 (2012).

Science Advances Manuscript Template Page 10 of 16

- 37. I. T. McCrum, M. T. M. Koper, The role of adsorbed hydroxide in hydrogen evolution reaction kinetics on modified platinum. *Nat. Energy.* **5**, 891–899 (2020).
- 38. P. Sun, M. V. Mirkin, Kinetics of electron-transfer reactions at nanoelectrodes. *Anal. Chem.* **78**, 6526–34 (2006).
- 39. Nioradze, R. Chen, J. Kim, M. Shen, P. Santhosh, S. Amemiya, Origins of nanoscale damage to glass-sealed platinum electrodes with submicrometer and nanometer size. *Anal. Chem.* **85**, 6198–6202 (2013).
- 40. W. Kohn, L. J. Sham, Self-consistent equations including exchange and correlation effects. *Phys. Rev.* **140**, A1133 (1965).
- 41. G. G. Kresse, J. J. Furthmüller, Efficient iterative schemes for ab initio total-energy calculations using a plane-wave basis set. *Phys. Rev. B*, **54**, 11169 (1996).
- 42. P. E. BlöChl, Projector augmented-wave method. *Phys. Rev. B.* **50**, 17953–17979 (1994).
- 43. G. Kresse, D. Joubert, From ultrasoft pseudopotentials to the projector augmented-wave method. *Phys. Rev. B.* **59**, 1758–1775 (1999).
- 44. J. Wellendorff, K. T. Lundgaard, A. Møgelhøj, V. Petzold, D. D. Landis, J. K. Nørskov, T. Bligaard, K. W. Jacobsen, Density functionals for surface science: exchange-correlation model development with bayesian error estimation. *Phys. Rev. B.* **85**, 235149–235149 (2012).
- 45. S. Grimme, Semiempirical GGA-type density functional constructed with a long-range dispersion correction. *J. Comput. Chem.* **27**, 1787–1799 (2006).
- 46. J.K. Nørskov, J. Rossmeisl, A. Logadottir, L. Lindqvist, J. R. Kitchin, T. Bligaard, H. Jónsson, Origin of the overpotential for oxygen reduction at a fuel-cell cathode. *J. Phys. Chem. B.* **108**, 17886–17892 (2004).

Acknowledgments

This work was supported by the U.S. National Science Foundation (CHE-1900401 to H.L.X. and 1900463 to M.V.M) and the start-up funding of H.L.X. This research used resources of the Center for Functional Nanomaterials, which is a U.S. Department of Energy (DOE) Office of Science Facility, a U.S. DOE Office of Science User Facility operated for the DOE Office of Science by Brookhaven National Laboratory under Contract No. DE-SC0012704. The XAFS spectra obtained from beamline TPS 44A at National Synchrotron Radiation Research Center (NSRRC) is appreciated.

Author contributions: H.L.X. conceived the idea. X.J.L. and H.L.X.co-supervised the project. L.L.H. designed experiments and analyzed data. X.J.L. performed electrochemical experiments and analyzed the electrochemical data. P.F.O. and J.S. conducted DFT calculations. W.L., L.L.H. and J.L. prepared catalysts as well as took and analyzed TEM images. X.W. and M.V.M. performed the SECM experiments and analyzed the SECM data. H.T.W., L.L.H., C.W.P. and W.F.P. took and analyzed the XAFS spectra. R.Z. fit the XANES and EXAFS spectra. All authors discussed the results and implications at all stages.

Competing interests: Authors declare no competing interests.

Data and materials availability: All data needed to evaluate the conclusions in the paper are present in the paper and/or the Supplementary Materials. Additional data related to this paper may be requested from the authors.

Science Advances Manuscript Template Page 11 of 16



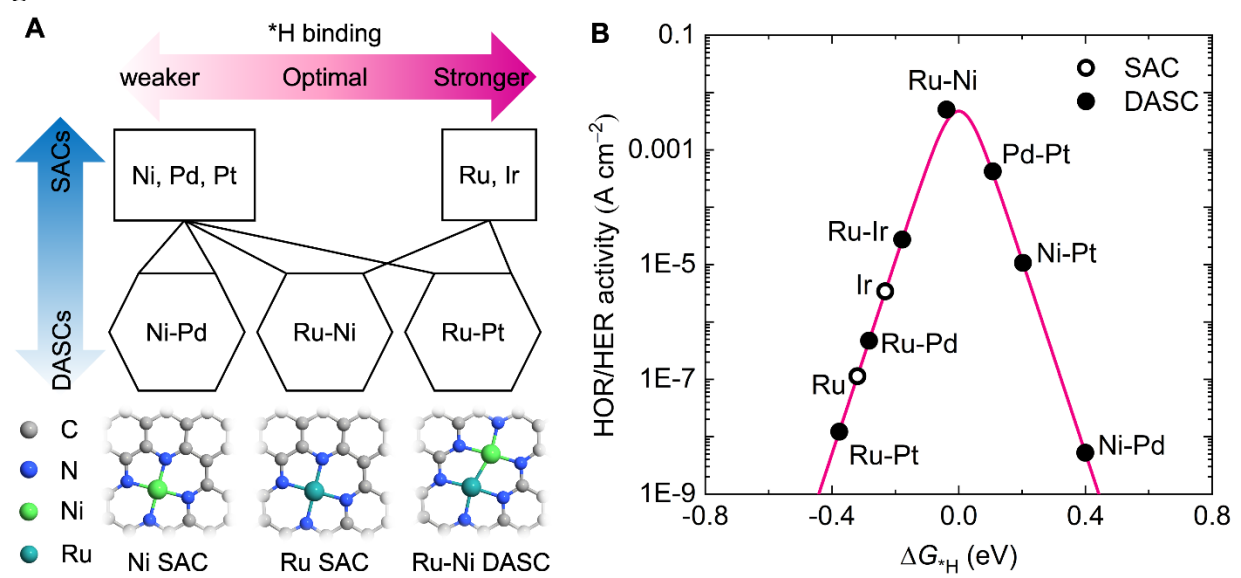


Fig. 1. Tuning the energetics of HOR reaction intermediates by diatomic site catalysts (DASCs). (A) Tuning of *H binding energy (ΔG_{*H}) via combination between various SACs by assuming the linear interpolation principle. The optimized structures of Ni SACs, Ru SAC, and Ru-Ni DASC are illustrated (cyan, Ru; green, Ni; blue, N; grey, C). (B) HOR activities of SACs and DASCs determined by BEEF-vdW calculations with the optimum value of ΔG_{*H} obtained for Ru-Ni DASC. We assume the transfer coefficient (α) equals to 1.0 in the simple mean-field, microkinetic model proposed in ref.³⁰ as an estimation of HOR/hydrogen evolution reaction (HER) activity (exchange current density, A cm⁻²). Some data points of SACs and DASCs are not included in this figure for a better visualization.

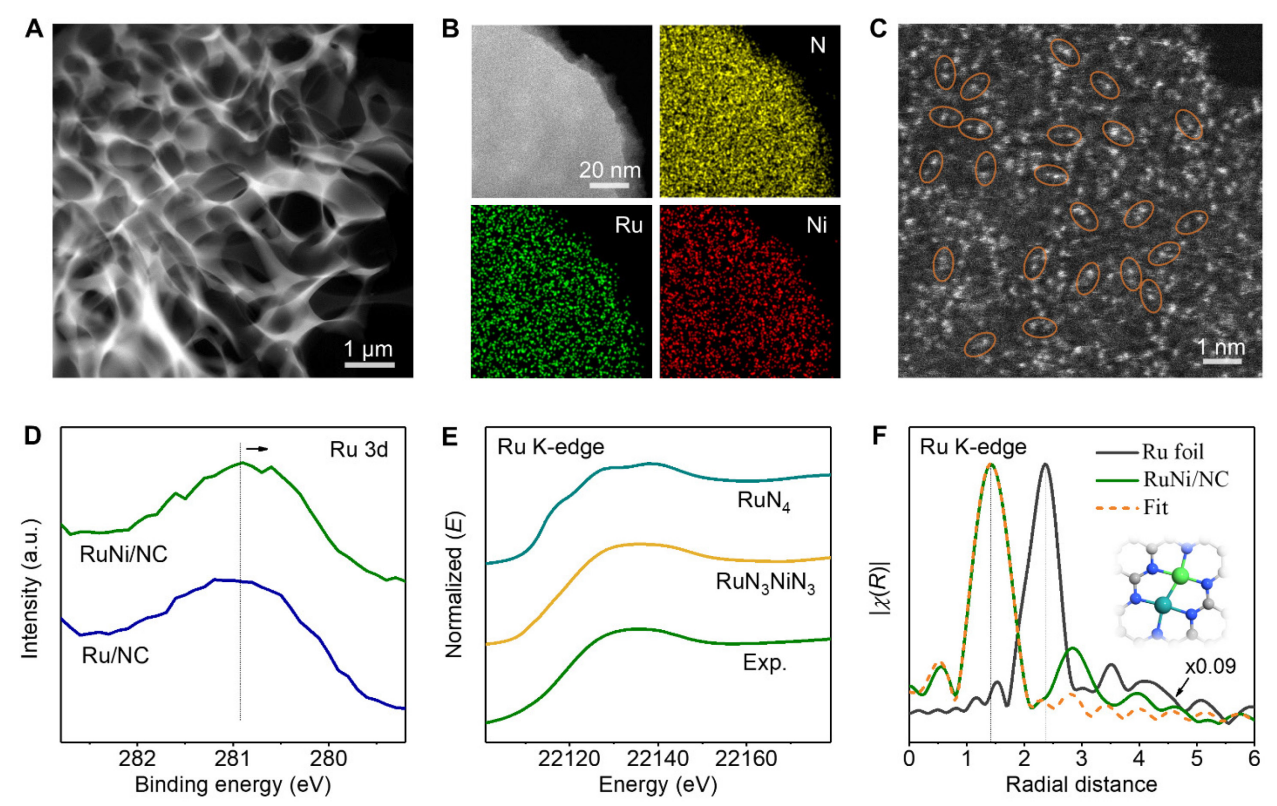


Fig. 2. Structural characterization of RuNi/NC. (**A**) Low-magnification HAADF-STEM image. (**B**) HAADF-STEM image and corresponding STEM-EDS elemental maps of N, Ru, and Ni. (**C**) Atomic-resolution HAADF-STEM image, in which some of Ru-Ni diatomic pairs are highlighted by orange ovals. (**D**) Ru 3d XPS spectra of RuNi/NC and Ru/NC. (**E**) Comparison between the experimental Ru K-edge XANES spectrum of RuNi/NC and the theoretical ones calculated based on the models of RuN₃NiN₃/graphene and RuN₄/graphene, which were generated after energy optimization. (**F**) Ru K-edge FT-EXAFS spectra of Ru foil, RuNi/NC, and the fit with the RuN₃NiN₃/graphene model. The inset is the corresponding atomic model.

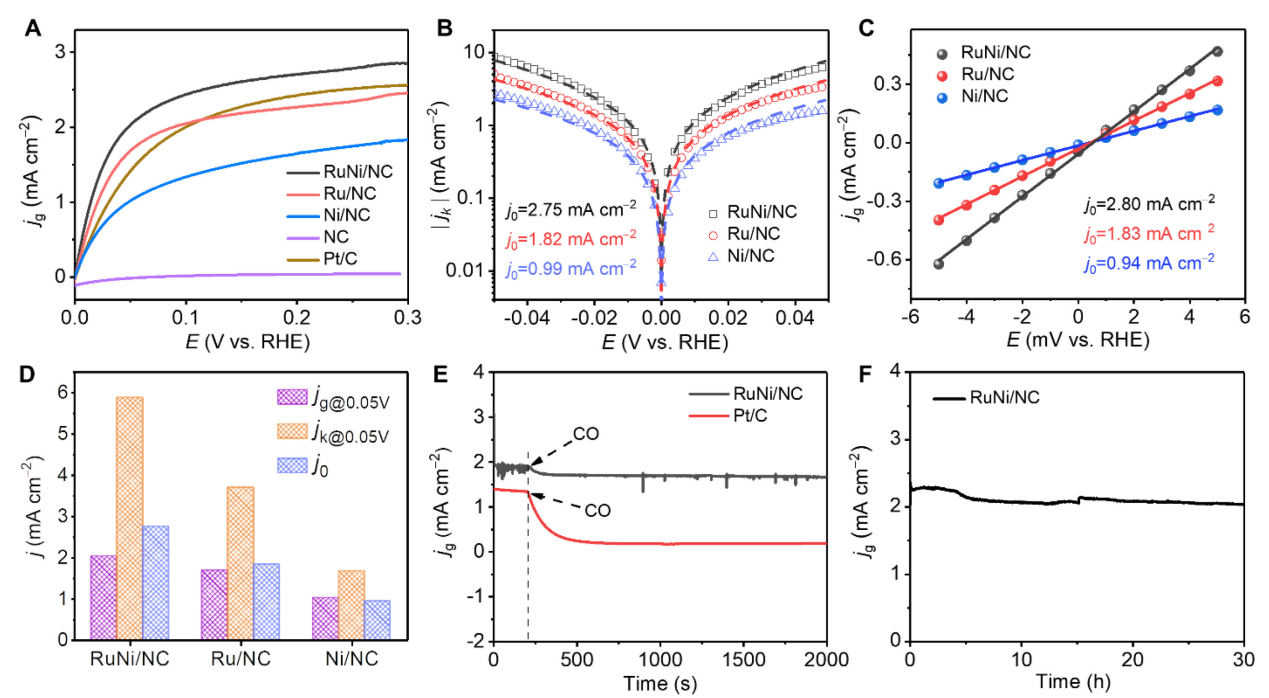


Fig. 3 | **HOR performances.** (**A**) Polarization curves of RuNi/NC, Ru/NC, Ni/NC, and Pt/C in H₂-saturated 0.1 M KOH at a scan rate of 1 mV s⁻¹ and rotating speed of 1,600 rpm. (**B**), HOR/HER Tafel plots of the kinetic current density on RuNi/NC, Ru/NC, and Ni/NC. The dash lines indicate the Butler–Volmer fitting. (**C**), Micropolarization region (–5 to 5 mV) of RuNi/NC, Ru/NC, and Ni/NC catalysts. (**D**), Comparison of $j_{g@0.05V}$, $j_{k@0.05V}$ and j_0 for RuNi/NC, Ru/NC, and Ni/NC. (**E**) Current density–time chronoamperometry response of RuNi/NC and Pt/C in H₂/200 ppm CO-saturated 0.1 M KOH solution at 50 mV. (**F**), Stability test of current density of Ru/NC during 30-h HOR at 50 mV. Note that j_g represents current density normalized by the geometric area of the electrode.

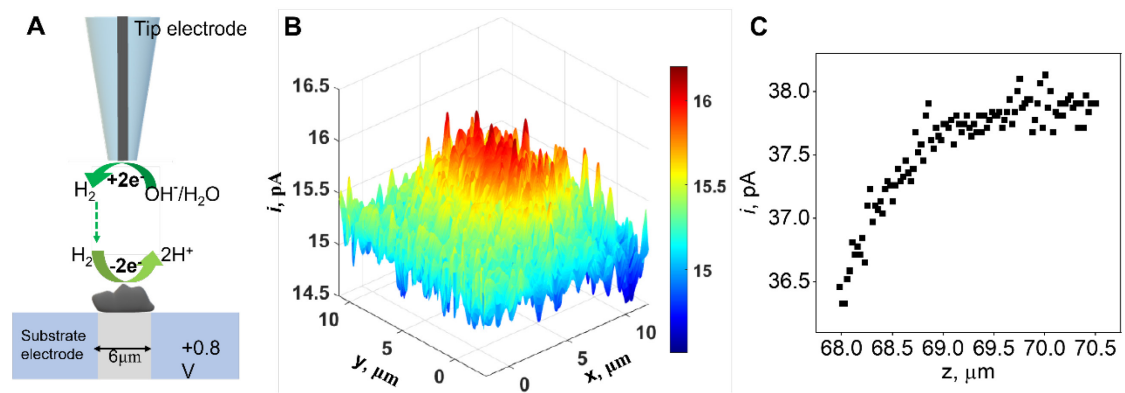


Fig. 4. SECM measurements of HOR activity of RuNi/NC and NC catalysts in basic solution. (A) Schematic representation of probing electrocatalytic activity for HOR of the RuNi/NC catalyst by Tip Generation-Substrate Collection (TG-SC) mode of SECM experiments; (B) SECM TG-SC mode image of the RuNi/NC sample. The solution contains 0.1 M PB (pH 10). $E_T = -1.2 \text{ V}$, $E_S = +0.8 \text{ V}$ vs. Ag/AgCl; (C) SECM approach curve recorded at the NC electrode in 0.1 M PB (pH 10). $E_{\text{sub}} = +0.8 \text{ V}$, $E_{\text{tip}} = -1.2 \text{ V}$ vs. Ag/AgCl.

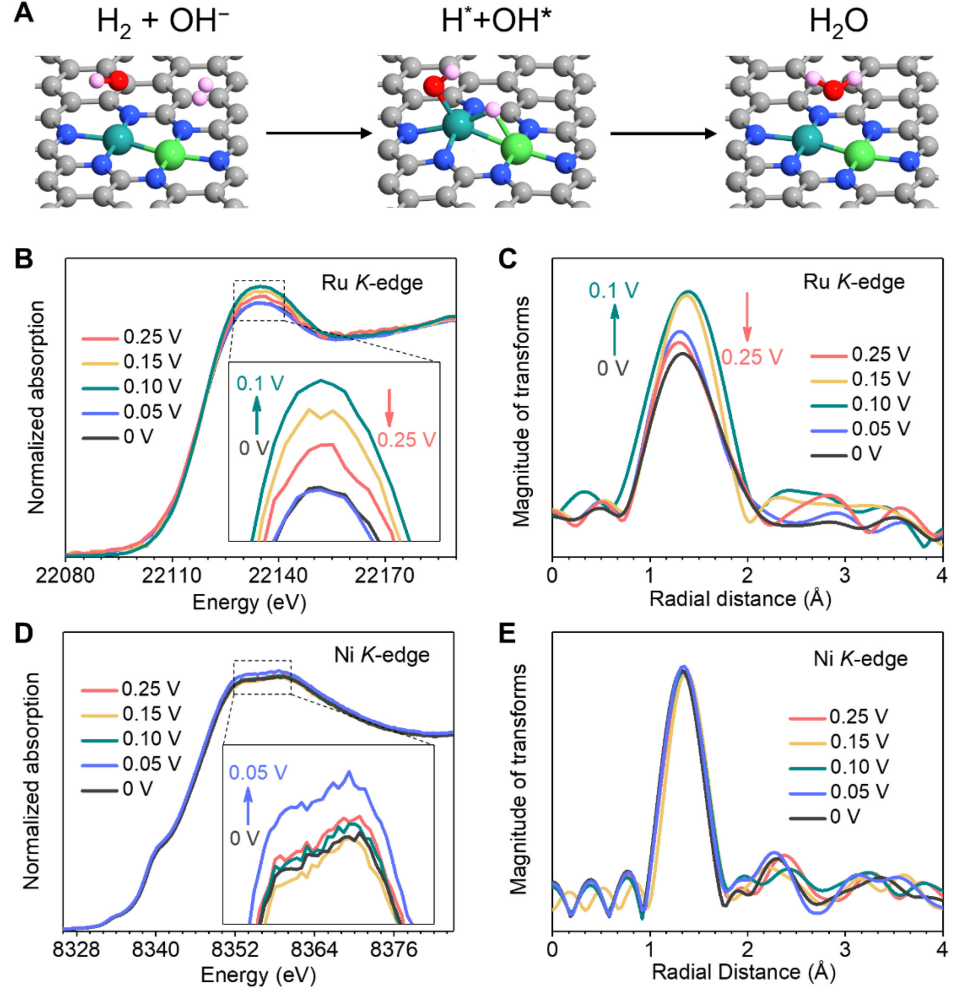


Fig. 5. HOR mechanism on RuNi/NC. (**A**) Schematic illustration of HOR on RuNi/NC obtained from DFT calculations. The pink, grey, blue, red, green, and dark cyan balls represent H, C, N, O, Ni, and Ru, respectively. (**B–E**) In-situ XAFS measurement on RuNi/NC during HOR at different applied potentials. (**B**, **C**) Ru K-edge XANES and FT-EXAFS spectra. (**D**, **E**) Ni K-edge XANES and FT-EXAFS spectra.